A Data-Driven Reduced Order Model of an Isolated Rotor

Nicholas J. Peters
Aerospace Engineer
NASA Ames Research Center
Moffett Field, CA, USA

Christopher Silva
Aerospace Engineer
NASA Ames Research Center
Moffett Field, CA, USA

John Ekaterinaris
Prof. Aerospace Eng.
Embry-Riddle Aeron. Univ.
Daytona Beach, FL, USA

ABSTRACT

There are numerous conceptual design stage rotorcraft analysis tasks which demand a high-fidelity and low cost method for rotor load distribution predictions. Considering Urban Air Mobility (UAM) vehicles aim to operate in close proximity to buildings and with unique rotor configurations, there is a significant challenge in quickly and accurately modeling rotors operating in complex, turbulent flow fields. One potential path for deriving a high-fidelity, low cost rotor model is with data-driven surrogate modeling. In this study, an initial investigation is taken to apply a proper orthogonal decomposition (POD) based reduced order model (ROM) for the purpose of pressure distribution prediction. In this study, a POD ROM was derived to produce distributed pressure predictions on rotor blades subjected to topology change due to variation in twist and taper ratio. Rotor twist was varied between $\mathbf{0}^\circ$, $\mathbf{10}^\circ$, $\mathbf{20}^\circ$, and $\mathbf{30}^\circ$ while taper ratio was varied between 1.0, 0.9, 0.8, and 0.7. All rotors consisted of a single blade. The POD ROM was validated for three demonstration cases; a high thrust rotor in hover, a low thrust rotor in hover, and a rotor in forward flight with a flight speed of $M = 0.1$. Results showed highly accurate distributed load predictions could be achieved at minimal computational cost. Computational cost for hovering blade surface pressure modeling was reduced from 12 hours on 440 cores to 10^{-5} seconds on a single core. For blade in forward flight cost was reduced from 20 hours on 440 cores to 0.6 seconds on a single core. For cases of high thrust and low thrust rotors, POD ROM was used to undergo a design optimization of the rotor such that figure of merit was maximized. Total optimization time for each case was 1 minute.

NOTATION

c	search direction
C_Q	coefficient of torque
C_T	coefficient of thrust
FM	figure of merit
M	free stream Mach number
M_{tip}	tip Mach number
n	retained subset of POD modes
$\tilde{s}$	summation of singular values
s_i	singular value i
$\mathbf{u}(\mathbf{x},t)$	snapshot matrix
$\bar{\mathbf{u}}(\mathbf{x})$	time-average of snapshot matrix
$\mathbf{u}(\mathbf{x},t)'$	perturbation matrix
$\mathbf{U}$	POD modes
$\mathbf{V}^T$	right-singular vectors of $\mathbf{u}(\mathbf{x},t)'$
λ	taper ratio
Ψ	twist
Φ_i	POD mode i
Σ	singular value matrix
σ	solidity

Presented at the VFS Aeromechanics for Advanced Vertical Flight Technical Meeting, San Jose, CA, January 25–27, 2022.

INTRODUCTION

It is common for rotorcraft analysis to include fluid-structure interactions, structural dynamics, vehicle component sizing, topology optimization, flight simulation, etc. For each of these tasks it is essential that there exist a model capable of providing load predictions to a high degree of accuracy for a variety of rotor configurations. One approach to obtaining these load predictions is through mid-fidelity design tools such as Comprehensive Analytical Model of Rotorcraft Aerodynamics and Dynamics (CAMRAD) (Ref. 1), Rotorcraft Comprehensive Analysis System (RCAS) (Ref. 2), or Comprehensive Hierarchical Aeromechanics Rotorcraft Model (CHARM) (Ref. 3). Through leveraging these analysis tools numerous sub-topics of interest have been investigated ranging from multi-rotor performance prediction (Refs. 4, 5) to aeroelasticity (Refs. 6, 7). When applied to the early stages of vehicle optimization, typically mid-fidelity tools provide an excellent path to obtaining a limited design space from which an optimal solution can be identified. Yet, there still remain significant limitations to mid-fidelity analysis tool-sets when applied to rotor operation in turbulent flow fields. These limitations become particularly pronounced once considering that many urban air mobility (UAM) rotorcraft will likely have rotors operating in highly turbulent flow fields, particularly those proposed to operate in multi-rotor configurations or in

close proximity to buildings. As more rotorcraft designs are beginning to account for these operating conditions, uncertainty in mid-fidelity tools has led to a broadening of optimal design spaces found in the early stages of the conceptual design process.

One potential solution for narrowing this design space is through applying computational fluid dynamics (CFD). Numerous solvers (mStrand (Ref. 8), SU2 (Ref. 9), OpenFoam (Ref. 10), etc.) have been developed to help streamline the process of rotorcraft CFD simulation. Through implementation of Large Eddy Simulation (LES) (Ref. 11) and Detached Eddy Simulations (DES) (Ref. 12) in CFD, numerical based studies of rotorcraft have shown to be capable of resolving flow fields relevant for performance and loads of isolated rotors in hover/forward flight (Ref. 13), during rotorcraft pitch up maneuvers (Ref. 14), and rotor-ship wake interactions (Ref. 15). Yet, despite significant advancements in both the hardware (Ref. 16) and software (Ref. 17) rotorcraft CFD simulations still prove to be too computationally expensive for many engineering tasks. For a complete comprehensive CFD analysis of a full scale rotorcraft, computational expense commonly requires simulation run times ranging from days to weeks (Ref. 18). For engineering tasks, which require hundreds if not thousands of iterations such as design optimization, full CFD modeling is not an option. It is this resource limitation which has led to a desire for a CFD-based surrogate model.

While currently available computational resources limit the number of CFD simulations during conceptual design to a few tens of runs, recent studies have shown that by retaining a truncated subset of dominate flow features a useful and meaningful reduced order model (ROM) can be constructed (Refs. 19, 20). While there exist many formulations of mode-based ROMs, in this study an interpolation based ROM will be presented. This ROM was constructed in a two step process. First, a low rank subspace is identified. This subspace can be found using a variety of modal decomposition methods such as Proper Orthogonal Decomposition (POD), Dynamic Mode Decomposition (DMD) (Ref. 21), Spectral Proper Orthogonal Decomposition (SPOD) (Ref. 22), etc. In this study, POD was utilized to identify a low rank subspace. Once a subspace was identified an interpolation scheme is then applied to make predictions. Recent work (Refs. 23–29) has shown that these ROM-based surrogate models are able to retain a high degree of fidelity while operating at minimal computational cost. Example of areas of ROM application include heat transfer, combustion, turbine blade modeling, boundary layer ingestion, and store separation.

While previous studies have applied POD ROMs to isolated bodies with varying inflow conditions, there is minimal application to modeling surface pressure distributions for three dimensional unsteady dynamic bodies, particularly once variation in surface topology is considered. A significant contributing factor for this absence of literature is that data-driven modeling relies heavily on the assumption that dominate physics for the system of interest are comprehensively captured in the training dataset. For this reason, many applications of CFD based data-driven ROMs, while valuable demonstrations, rely on either two-dimensional flows (airfoil load prediction (Ref. 30)), steady-state assumptions (supersonic flows (Ref. 31)), or systems where symmetry/periodicity can be leveraged (rotor-stator modeling (Ref. 32)) such that CFD computational expense is minimized and the number of sample points can be maximized. For rotorcraft based applications of CFD based data-driven ROMs computational expense is comparatively large resulting in minimal sampling of the domain. As such, the POD ROMs demonstrated in this study will need to extract meaningful information from a relatively small number of samples.

Typically, there are two ways in which a parametric interpolation based POD ROM could fail to produce meaningful predictions. The first potential situation could be through the POD algorithm being incapable of representing the space with a limited expansion of modes. While ultimately POD mode retention could be expanded to several hundreds, if not thousands, of modes these high mode counts often result in more challenging interpolations. Typically, while initial POD modes can smoothly be correlated to design parameters higher mode numbers are often more stochastic resulting in more challenging interpolations. The other way a POD ROM may fail to provide accurate predictions is through under-sampling a sufficiently non-linear design space. If a design space is found to be too non-linear, then the total number of CFD simulations required to derive a model may no longer warrant the construction of a ROM.

To investigate POD ROM capability in the field of rotor pressure load predictions, a POD ROM was derived and tested under three basic operating conditions for a single, isolated blade. In each case, design space complexity is increased to test reconstruction and interpolation capability. The first ROM this study will present models a high thrust isolated rotor blade in hover. The rotor blade's taper ratio and twist was varied to construct 16 CFD simulations using the OVERFLOW solver (Ref. 33). A POD ROM was constructed from these cases, validated against an additional 3 CFD simulations, and then employed to achieve a design optimization of the rotor blade. This process was repeated again for a low thrust isolated rotor blade in hover. With both high and low thrust rotor cases, figure of merit, coefficient of thrust, and coefficient of torque will be used as metrics for ROM prediction accuracy. For the final ROM, the study modeled an isolated rotor blade in forward flight given the same variations in taper ratio and twist. This ROM was also validated against 3 additional CFD simulations. Integrated sectional coefficient of thrust was used as the metric of forward flight ROM prediction accuracy. With these three ROMs, the study aims to provide insight into the capabilities of POD ROMs for distributed load predictions given a variation in blade shape over a variety of standard rotor operating conditions.

NUMERICAL APPROACH

Before this study could begin, a procedure was required for efficiently generating rotor blade grids given a linear variation in taper ratio and twist. This procedure was necessary not only for generating grids for CFD simulation, but also for applying POD ROM for an iterative design optimization. As such, a procedure was developed over the course of this study which allows for a parametric definition of rotor blades. The procedure starts by reading a single input file which holds the definition of rotor blade's twist (Ψ), taper (λ), sweep, dihedral, and airfoil cross section at a number of span-wise stations. These input file formats can either be National Aeronautics and Space Administration (NASA) Design and Analysis of Rotorcraft (NDARC) (Ref. 34) geometry files or CAMRAD input files. A PLOT3D (Ref. 35) file is then generated for the rotor's Cartesian surface grid. With the meshing algorithm defined, the study began generating the 16 blades, as defined in Table 1 and 3 validation grids, as outlined in Table 2. Each blade consisted of 276 chord-wise and 128 span-wise nodes for a total surface cell count of 34,944. All 16 blades had a mean chord of 1 ft and a radius of 10 ft. Examples of blades from cases **c1** and **c16** can be seen in Figure 1.

Each rotor was limited to a single blade to simplify rotor geometry and limit the influence of variables not represented in the POD ROM from affecting blade pressure distributions. It should be noted that this geometric constraint is not consistent with blade counts found on rotorcraft and thus typical rotor performance may not be represented in the current study. Nonetheless, this geometric constraint still allows for pressure distributions representative of those found for blades in hover and forward flight to be modeled. The selected geometries produce a constrained domain within which a POD ROM can be tested for capabilities to reconstruct typical load distributions found on blades and model their evolution as a blade's twist and taper ratio varies.

To generate caps for the rotor's root and tip faces, the Chimera Grid Tools' (CGT's) WINGCAP software was used (Refs. 36, 37). The CGT is a tool-set developed by NASA for the purpose of pre- and post-processing of chimera overset grids (Ref. 38), particularly for use in NASA's OVERFLOW CFD solver. An example of a grid generated for the rotor's tip cap can be seen in Figure 2. Volume grids were generated from the surface meshes using CGT's hyperbolic grid generator HYPGEN (Ref. 39) software. An example of the HYPGEN generated extrusion is shown in in Figure 3. Total near body volume cell count for each case is 3.5 million. Normal spacing at the surface was at a y+ of 1 and growth was limited to a rate of 1.2. A Cartesian background mesh was then constructed with pressure farfield boundary conditions extending 15 rotor radii from origin. The SAMcart solver was used for the background mesh.

For numerical simulation, the study used the CFD solver OVERFLOW (Ref. 40). OVERFLOW is a CFD solver developed by NASA and uses a series of structured, overset grids to model fluid flows. For turbulence modeling, the single equation Spalart-Allmaras model was used with curvature corrections (Ref. 41). Second order temporal and spatial accuracy was used. To assist in case setup, the CREATE-AV Helios modeling tool was used (Refs. 42,43). The Helios code takes a modular approach to numerical simulation where users are allowed to interchange meshing and solver algorithms and thus allows for a broader flexibility for the code to be applied to a variety of topics (Refs. 44–46). For the hovering rotor cases, 5 startup revolutions were completed before extracting rotor surface pressures. For the forward flight cases 8 rotor revolutions were completed before extracting rotor surface pressures. Startup revolutions were selected such that periodic solutions were obtained. Clearly, because of these requirements the cost of the CFD simulations is high. Each forward flight CFD simulation required 12 hours to compute on 440 cores.

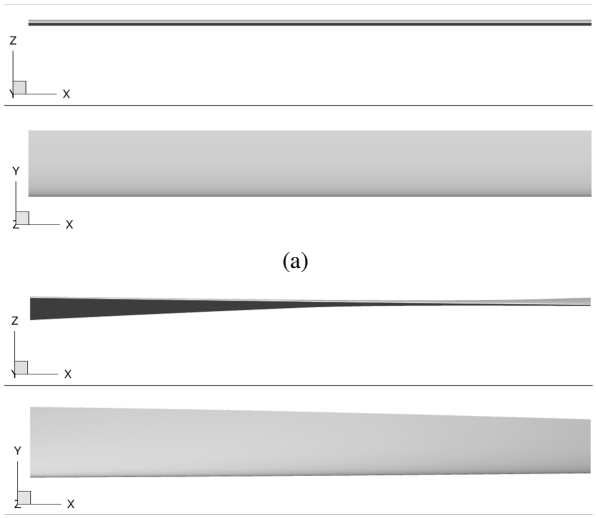

Figure 1: Comparison of two geometries used in this study. Image (a) shows $\Psi = \mathbf{0}^\circ$ & $\lambda = 1.0$. Image (b) shows $\Psi = \mathbf{30}^\circ$ & $\lambda = 0.7$.

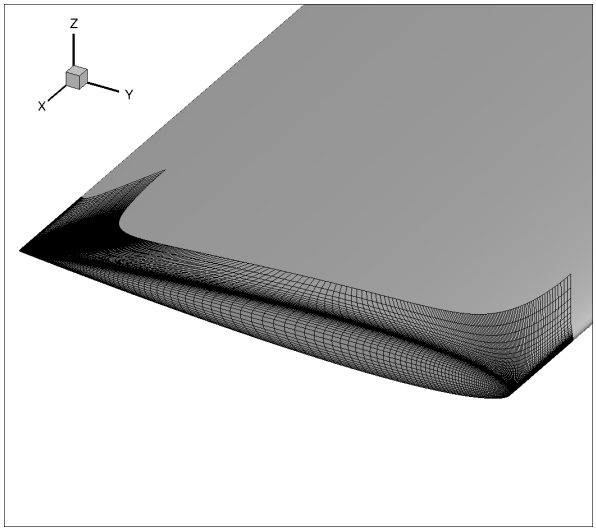

Figure 2: Example of tip cap surface mesh.

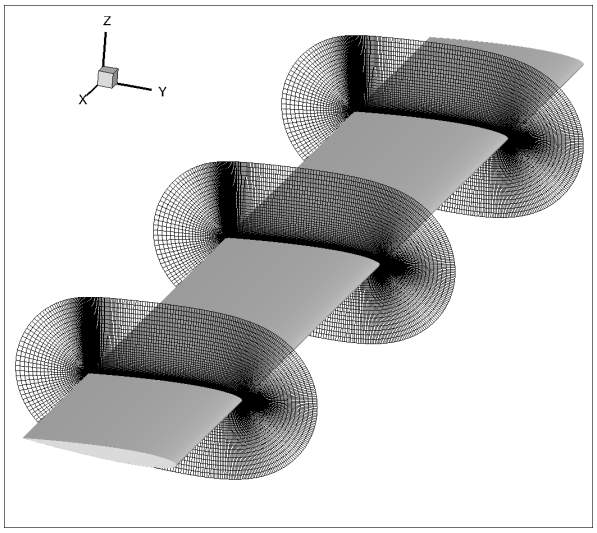

Figure 3: Example of blade volume mesh. Shown with slices of volume mesh at radial positions of x/R = 0.30, 0.57, and 0.86.

For the high thrust hovering rotor, 16 CFD simulations covering geometries outlined in Table 1, were completed with a fixed collective of 8°. These cases were used to construct the first POD-ROM. This ROM was then validated against the three additional validation rotor geometries outlined in Table 2. For the low thrust hovering rotor, CFD simulations were again completed covering geometries outlined in Table 1 with a fixed collective of 4°. A POD ROM-based surrogate model was constructed and validated for all three validation geometries. For rotor in forward flight the same simulations were completed with a fixed collective of 4° and free stream flow of $M = 0.1$ moving in the positive x-axis direction. For all CFD simulations a tip Mach number of $M_{tip} = 0.5$ was used. For this study, no cyclic motion was defined for the blade.

Table 1: The below matrix summarizes the 16 geometries used in this study.

		Twist(deg) Ψ			
		0°	10°	20°	30°
	1.0	***c1***	***c2***	***c3***	***c4***
	0.9	***c5***	***c6***	***c7***	***c8***
	0.8	***c9***	***c10***	***c11***	***c12***
Taper Ratio λ	0.7	***c13***	***c14***	***c15***	***c16***

Table 2: The geometries used for validation of POD-ROM.

Geometries	Twist (deg)	Taper
v1	15°	1.0
v2	0°	0.85
v3	15°	0.85

For both the high and low thrust rotor cases, a POD ROM was used to optimize the blade's twist and taper ratio such that figure of merit (FM) would be maximized. To undergo this optimization, three blade surface grids were first generated. The first grid was generated using the current iteration's solution for optimal twist and taper ratio. Two additional grids were then generated, the first used a 0.1% increase in twist while the second used a 0.1% increase in taper ratio. Solutions for distributed pressures were solved using the derived POD ROM from which loads were integrated and used to solve for FM of each blade. First derivatives for FM with respect twist and taper ratio were solved using a first order Euler approximation and used to select new optimal twist and taper ratio through usage of steepest descent algorithm. A criteria of 0.1% change in solution was selected as stopping condition. An overview of the design optimization pipeline used in this study is presented in Figure 4. In this figure, (Ψ^k, λ^k) is the current optimal solution, $(1.001 * \Psi^k, \lambda^k)$ is used to find first derivative of FM with respect to Ψ, and $(\Psi^k, 1.001 * \lambda^k)$ is used to find first derivative of FM with respect to λ. Optimal solution used for the next step is $(\Psi^{k+1}, \lambda^{k+1})$

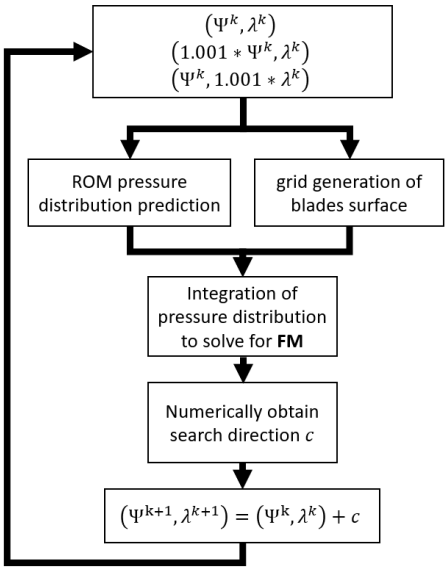

Figure 4: Overview of design optimization pipeline used in this study.

In this study, FM was computed using Eq. 1. To compute both coefficient of thrust, C_T, and coefficient of torque, C_Q, blade distributed surface pressure solutions were numerically integrated. For rotor in forward flight, integrated sectional coefficients of thrust were plotted from azimuth 0° to 360°. While viscous CFD solutions were obtained in this study, shear stresses were not utilized when computing integrated loads for either POD ROM or CFD. Given that the objective of this study was to provide an initial investigation of POD ROM distributed load prediction capability for rotor blades, expanding POD ROM to include multi-directional shear loads was not warranted in the current work.

$$FM = \frac{C_T^{3.0/2.0}}{C_Q\sqrt{2.0}} \tag{1}$$

ROM APPROACH

In this section of the paper, the methodology for ROM construction will be reviewed. The ROM method used in this study consisted of two steps. First modal decomposition method will be reviewed. Next, interpolation method used in this study will be reviewed.

Proper Orthogonal Decomposition

The POD, which itself is a variation of the Principle Component Analysis (PCA) (Ref. 47), was introduced as a method for extracting a low dimensional subspace which captures the majority of the variance, often referred to as energy, from the full phase space (Ref. 48). While there exist numerous formulations for POD, in this paper the snapshot method as introduced by Sirovitch (Ref. 49) will be used. In this approach any scalar of the flow field can be represented by the sum of the scalar's time-average, $\bar{\mathbf{u}}(\mathbf{x})$, and n orthonormal POD modes $\Phi_i(\mathbf{x})$ times the temporal coefficient $\mathbf{a}_i(t)$. In this study, surface pressure solutions were used to formulate the snapshot matrix. The relationship is shown below, where $\mathbf{a}_i(t) =< (\mathbf{u}(\mathbf{x},t) - \bar{\mathbf{u}}(\mathbf{x})), \Phi_i^T(\mathbf{x}) >$.

$$\mathbf{u}(\mathbf{x},t) = \bar{\mathbf{u}}(\mathbf{x}) + \sum_{i=1}^{n} \mathbf{a}_i(t)\Phi_i(\mathbf{x}) \tag{2}$$

To obtain $\Phi_i(\mathbf{x})$ the a snapshot matrix $\mathbf{u}(\mathbf{x},t)$ is first formed. In this matrix, the row space holds spatial information while the column space holds temporal information. The perturbation matrix, $\mathbf{u}(\mathbf{x},t)'$, is calculated by subtracting out the snapshot matrix's time-average. The POD modes are then found through a single value decomposition (SVD) of $\mathbf{u}(\mathbf{x},t)'$, where the subset of modes Φ_i are extracted from $\mathbf{U}$. In Eq. 3, $\mathbf{U}$ contains the eigenvectors for $\mathbf{u}(\mathbf{x},t)'$ times it's transpose, $\mathbf{V}^T$ contains the eigenvectors of the transpose of $\mathbf{u}(\mathbf{x},t)'$ times itself and Σ contains the singular values of the SVD.

$$\mathbf{u}(\mathbf{x},t)' = \mathbf{U}\Sigma\mathbf{V}^T \tag{3}$$

The process of reducing dimensionality of the data-set down to a low rank subspace has been described in numerous publications (Refs. 48, 50). For the present study, the process of selecting an adequate subspace was based on energy retention. For this approach, the number of modes which must be retained is dependent on the behavior of the singular values, s, found in the diagonal of the Σ matrix. Given that s is little more than the square of the eigenvalues of $< \mathbf{u}(\mathbf{x},t)', \mathbf{u}(\mathbf{x},t)'^T >$, this then serves as a representation for how much of the snapshot matrix's energy is being captured by each mode. The amount of energy being captured in each mode can then be visualized by plotting the ratio of each singular value s_i to the sum of s denoted at $\tilde{s}$. The objective is then to retain a subset of modes, n, such that the below equation is satisfied.

$$\sum_{i=1}^{n} \frac{s_i}{\tilde{s}} \approx 1 \tag{4}$$

Once a POD model of the form of Eq. 2 had been constructed for the surface loads of various cases, an interpolation scheme is needed in order to make use of these modes for intermediate case predictions.

2-D Surface Map Interpolation

In order to produce a continuous representation of the temporal coefficients a two-dimensional mapping was constructed. During the construction of these mappings, the objective was to produce a continuous representation for the temporal coefficients. This continuous representation was provided by relating twist Ψ and taper ratio λ to the temporal coefficients $\mathbf{a}_i(t)$.

$$\mathbf{a}_i(t) = F(\lambda, \Psi) \tag{5}$$

Note that for the 2-D surface mapping method, it is an inherent requirement that the two variables selected combine to produce a unique definition of each snapshot. In the case of this study, selection of interpolation parameters becomes trivial. By selecting λ and Ψ as the mapping variables, any location on the snapshot matrix could be uniquely identified and a spline surface could be fit for each mode temporal coefficients. The advantage is that this method is relatively simple, accurate, and computationally inexpensive to setup. There is no training requirement as in neural networks, or large matrix inversions to make, and the user has a much greater degree of control over how the mapping can be constructed — whether a polynomial, linear, or logarithmic fit depending on the prior knowledge of the problem in hand.

RESULTS AND DISCUSSION

In this section the results for CFD simulation, POD ROM reconstruction and validation will be presented. Results are primarily split between the three demonstration cases; high thrust, low thrust, and forward flight. These three sections will be further split into three additional sections showing CFD simulation results, POD ROM reconstruction results, and POD ROM validation results.

High Thrust Rotor

In the first scenario of POD ROM rotor blade modeling, a high thrust rotor is used. With this demonstration case, the study was able to first test for the most basic operation conditions of which a POD ROM would be required to model. Thrust is

kept high which helps convect rotors wake downstream, thus contributing in a smaller degree of influence to the overall rotor pressure distributions. Coefficient of pressure distribution for case **c4** ($\lambda = 1.0, \Psi = 30^\circ$) is shown in Figure 5. From these pressure distribution, it can be seen that spanwise gradients are minimal. This allows for a relatively simple case for a POD ROM to be derived and applied to make predictions. Gradients are overall kept low, which typically results in fewer modes required to reconstruct the system. This is in contrast to low thrust rotor modeling where distributed loads vary to a larger degree in the spanwise direction caused by the blade's wake being convected away at a slower rate. However, even in the simplified case of the high thrust rotor there are still important characteristics the POD ROM must model with a limited mode count. Namely, these challenges are strong pressure gradients at rotor's leading edge along with a spanwise varying stagnation location. To obtain accurate predictions for C_T, C_Q, and FM these distributed loading characteristics must be modeled with a high degree of fidelity.

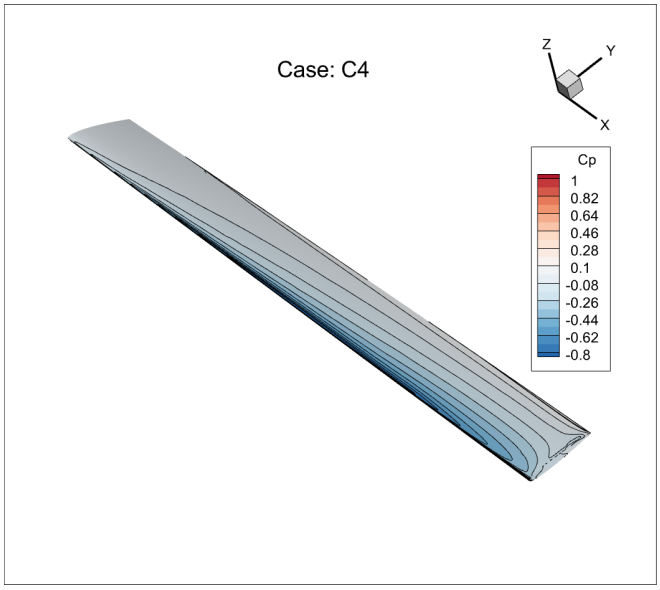

Figure 5: Surface pressure coefficient distributions for a high thrust rotor blade in hover. Blade geometry is defined by case **c4** ($\lambda = 1.0, \Psi = 30^\circ$).

Once all 16 blade geometries had been simulated, loads were integrated to obtain coefficient of thrust C_T, coefficient of torque C_Q, and figure of merit FM. These loads are plotted as functions of λ and Ψ in Figure 6. Results show that for C_T, C_Q, and FM there is a nonlinear relationship with Ψ while there is an almost linear relationship with λ. This characteristic of having multiple variables with widely varying degrees of influence on the system is commonplace for many practical rotorcraft applications including hysteresis modeling, aeroelasticity, controls, etc. If a multi-variable data-driven model is to be successfully derived for rotorcraft applications it must be capable of efficiently extracting the relationship each design variable has with rotor surface loads, whether that relationship be linear, quadratic, logarithmic etc.

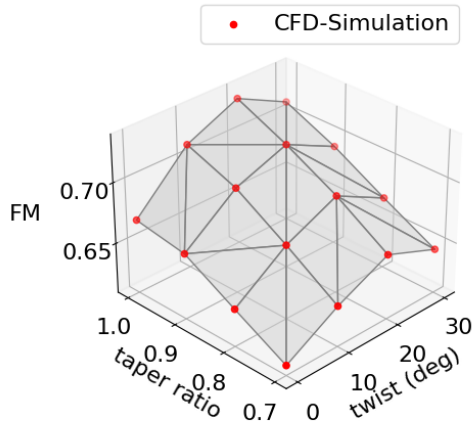

(a) FM

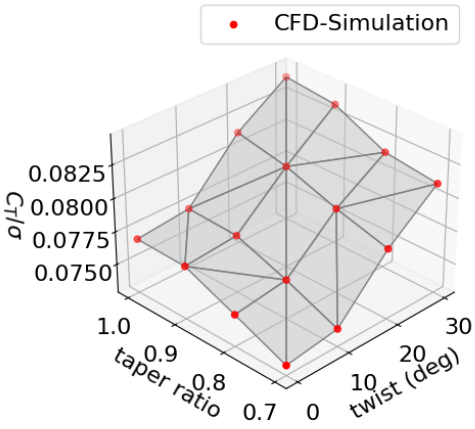

(b) $\frac{C_T}{\sigma}$

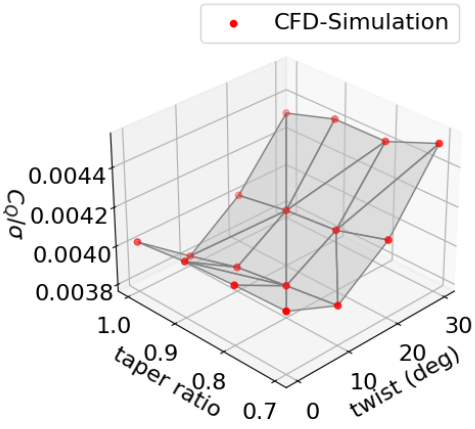

(c) $\frac{C_Q}{\sigma}$

Figure 6: Surface plot of FM, $\frac{C_T}{\sigma}$, and $\frac{C_Q}{\sigma}$ with respect to Ψ and λ as computed through CFD. Results are shown for all 16 cases outlined in Table 1.

ROM Reconstruction After completing all 16 high thrust hovering rotor simulations, solutions for surface pressure were compiled to form a single snapshot matrix. The POD algorithm was then used on this snapshot matrix after which it was iteratively determined that only 8 POD modes were required to produce mode count retention independent reconstructs of the blade's load distributions. In comparing load reconstruction capabilities for case **c4** between Figures 5 and 7 it can be seen that loads are being modeled with a high degree of fidelity in comparison to CFD. Spanwise pressure distribution is being correctly accounted for with the reduced representation. Maximum percent error between CFD and ROM surface pressures for all 16 reconstructions was 1%.

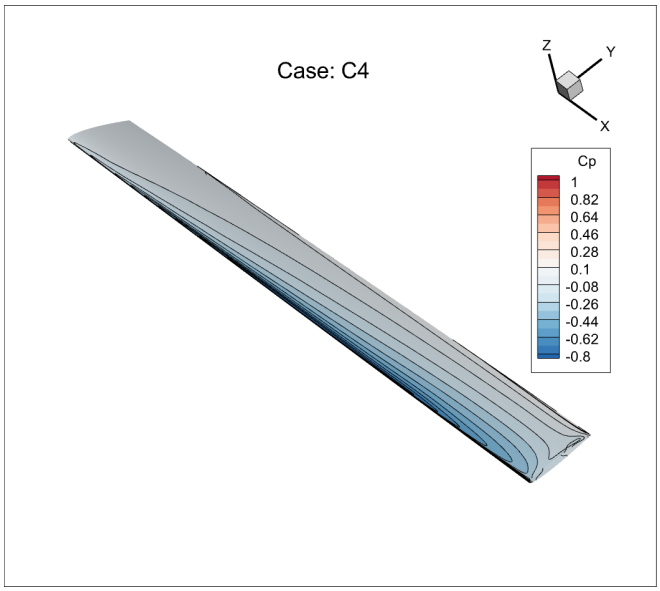

Figure 7: Coefficient of pressure distribution for case **c4** obtained by POD ROM.

Once these loads are integrated it is shown that a near exact representation of rotor load distribution is achieved with a minimum mode count. All parameters of interest, namely C_T, C_Q, and FM, are being accurately modeled through both variation in Ψ and λ. It should be noted that largest relative error during reconstruction was found for C_Q reconstructions. This deviation hints that the largest errors in reconstruction are occurring towards the blade's leading edge which would be consistent with previous applications of POD ROM's in literature. Historically, large gradients are challenging to model through modal decomposition with minimum mode retention counts. Yet, despite these challenges the results of this study show that leading edge gradients are captured with sufficient accuracy that C_Q is still being modeled with a high degree of fidelity. What remains to be shown is the capability of this ROM to not simply make accurate reconstructions of the dataset, but also make accurate predictions with new combinations of Ψ and λ as outlined in Table 2 such that a design optimization can be performed.

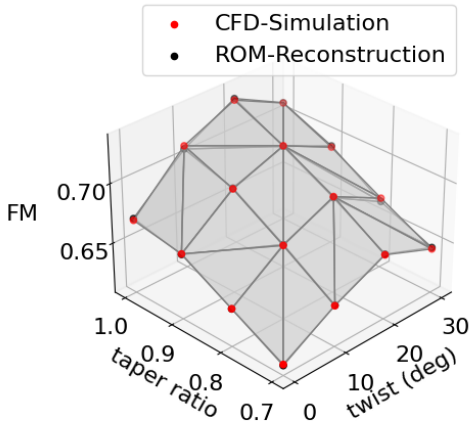

(a) FM

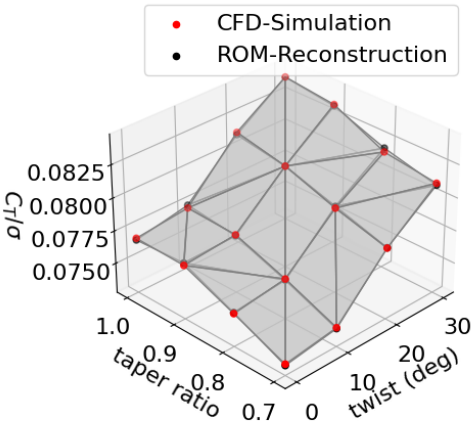

(b) $\frac{C_T}{\sigma}$

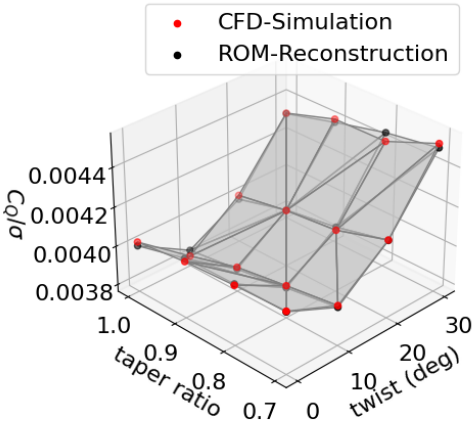

(c) $\frac{C_Q}{\sigma}$

Figure 8: Surface plot of FM, $\frac{C_T}{\sigma}$, and $\frac{C_Q}{\sigma}$ with respect to Ψ and λ as computed through CFD and POD ROM. Results are shown for all 16 cases outlined in Table 1.

ROM Validation After constructing the POD ROM and comparing reconstructing capabilities to CFD solutions, the study then moved to quantifying POD ROM predictive capabilities for the geometries outlined in Table 2. When comparing surface pressure distributions, shown in Figure 9, it was found that with a minimum mode count the POD ROM was capable of providing full distributed load predictions for all three validation cases. Surface pressure predicted error was largely limited to a narrow region on the rotor's tip and never exceeded 1.5% error compared to the CFD simulation.

Predicted surface pressures were then integrated to find FM,C_T, and C_Q. When comparing POD ROM predicted load coefficients to CFD it was found that for all three validation cases percent error never exceeded 1%, thus providing strong evidence that a POD ROM can be efficiently deployed to model a rotor blade's full distributed load with a high degree of fidelity. Summary of prediction capabilities for POD ROM is shown in Table 3. This POD ROM was also shown to make highly accurate predictions at minimal computational cost. For the high thrust rotor case, surface pressures as computed by CFD required 12 hours of compute time across 440 cores. Meanwhile the POD ROM was capable of making comparable predictions of surface pressures in just 10^{-5} seconds on a single core.

Given this massive reduction in computational expense, it became possible to directly apply this POD ROM to a design optimization of the rotor blade to derive a local maximum of FM. To demonstrate that the POD ROM could be quickly deployed for blade optimization applications the algorithm outlined in Figure 4 was used. In this algorithm, a POD ROM was used for surface pressure predictions while the grid generation algorithm constructed during this study was deployed for updating a blade grid at each iteration. Initial starting geometry was $\Psi = 15^\circ$ and $\lambda = 0.85$. Results showed that a optimal geometry of $\Psi = 21.5^\circ$ and $\lambda = 1.0$ could be found while taking 1 minute of compute time on a single core. A total of 20 iterations were required to obtain the optimal solution. These results show that by sampling a given design space a POD ROM can be efficiently derived such that a low cost and accurate model of the blade's surface pressures can be obtained and practically deployed.

Table 3: Summary of percent errors in coefficient of thrust, torque, and figure of merit predictions using POD ROM.

Geometries	C_T	C_Q	FM
v1	0.47%	0.62%	0.09%
v2	0.03%	0.81%	0.77%
v3	0.80%	0.84%	0.37%

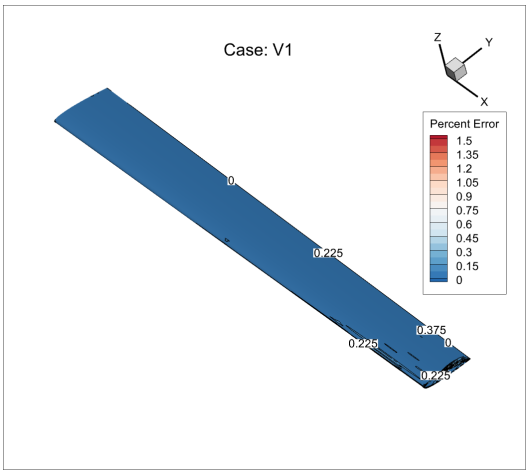

(a) **v1**

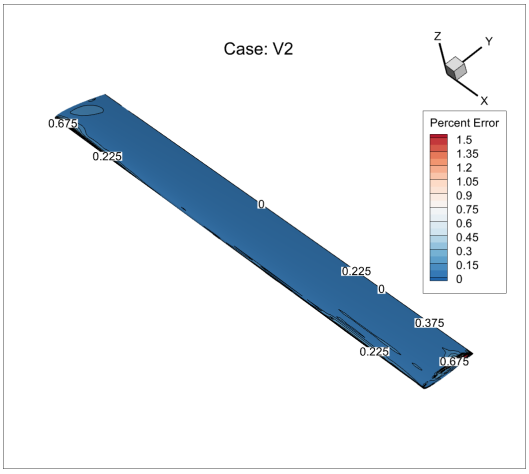

(b) **v2**

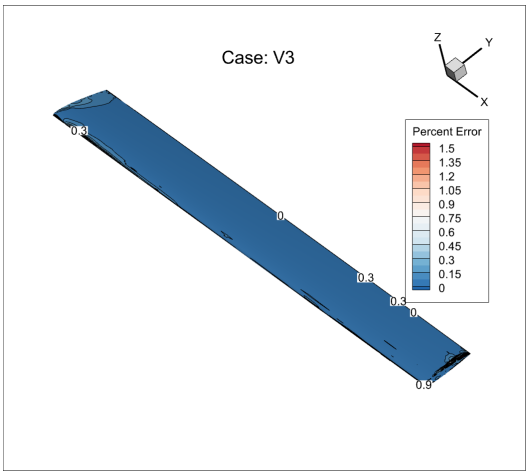

(c) **v3**

Figure 9: Percent error distributions for POD ROM surface pressure predictions with respect to CFD for all three validation cases.

Low Thrust Rotor

Up to this point, it has been shown how a POD ROM can be derived for a high thrust rotor operating in hover. While

these results provide evidence that POD ROMs can be a useful tool when modeling specific rotor blade design spaces, there were limitations to this specific application. As was previously identified, for high thrust rotors the wake holds a limited influence in rotor pressure distributions, being largely held to a narrow section of the rotor's tip. Yet for low thrust rotors, the wake is convected at a slower rate resulting in a stronger influence in the rotor's pressure distribution. Thus, through the low thrust rotor condition this study demonstrates an incremental increase in modeling complexity and it's influence on POD ROM's prediction capabilities.

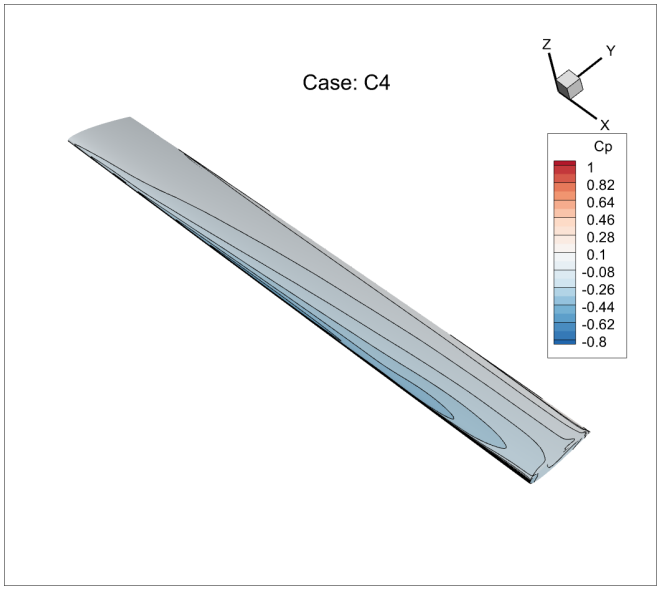

Figure 10: Coefficient of pressure distributions for a high thrust rotor blade in hover. Blade geometry is defined by case **c4** in Table 1.

In addition to the more complex pressure distribution, we see that integrated loads vary in a more complex pattern when compared to the high thrust rotor. When observing surface plots for FM, Figure 11, gradients with respect to Ψ are relatively smooth when compared to Figure 6. In addition, for the high thrust rotor maximum FM can continuously be found near $\Psi = 20^\circ$ as λ goes from $\lambda = 1.0$ to $\lambda = 0.7$, as shown in Figure 6. However, for the low thrust rotor FM, Figure 11, it is shown to be both represented as a less smooth gradient surface with respect to Ψ and have a varying local optimal Ψ value as λ goes from 1.0 to 0.7. When $\lambda = 1.0$ local optimal Ψ is found to be around $\Psi = 10^\circ$ while $\lambda = 0.7$ results in a local optimal Ψ of $\Psi = 30^\circ$. These results also shown an increase in non-linear influence for λ in the FM surface plot. While this increase in non-linearity will not lead to difficulties in reconstruction capabilities of POD ROM, it will ultimately create a more challenging modeling requirement for POD ROM to produce accurate predictions.

ROM Reconstruction With all 16 CFD simulations of the low thrust rotor completed, the study moved to first reconstruct the simulated surface pressures with a minimum mode

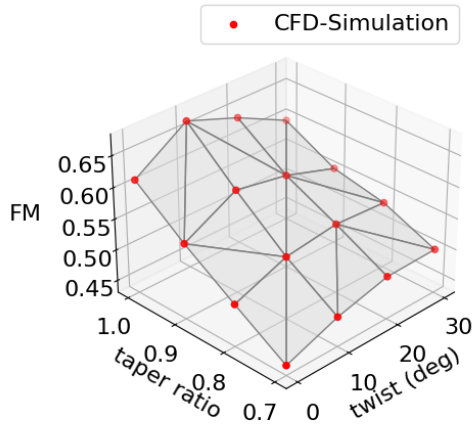

(a) FM

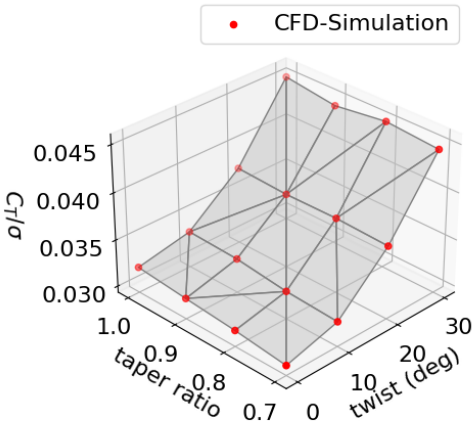

(b) $\frac{C_T}{\sigma}$

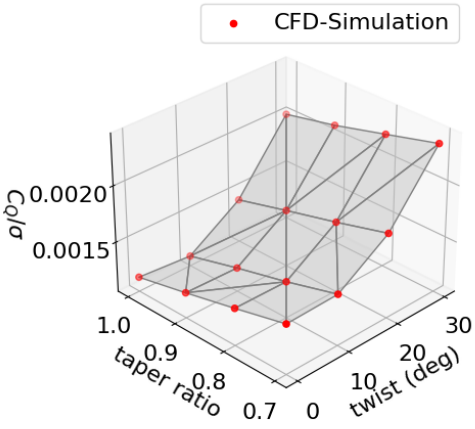

(c) $\frac{C_Q}{\sigma}$

Figure 11: Surface plot of FM, $\frac{C_T}{\sigma}$, and $\frac{C_Q}{\sigma}$ with respect to Ψ and λ as computed through CFD. Results are shown for all 16 cases outlined in Table 1.

count. It was found that POD ROM solution independence could be achieved through retention of only 8 POD modes. Once again, with the minimal mode retention count an excellent representation of the rotor's surface pressures could be achieved. Results in Figure 12 show that an almost exact reconstruction of surface pressures is achieved in comparison to Figure 7. Further observation of integrated loads for all 16 cases, as shown in Figure 13, highlight that efficient distributed load representation is achieved through POD.

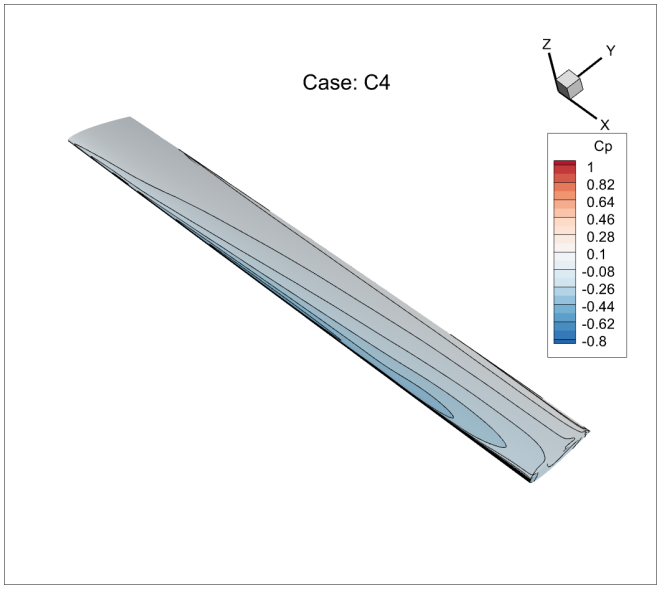

Figure 12: Coefficient of pressure distribution for case **c4** obtained by POD ROM.

These findings provide an important insight into POD ROM rotor modeling. Typically, when working with POD ROM's there are two potential ways in which a ROM will fail to generate an accurate representation. One potential failure point is through an inability to accurately represent the subspace through a low mode retention count. While often it is possible to extend POD mode retention count to many hundreds of not thousands of POD modes to obtain a more accurate reconstruction, higher mode retention counts provides a significant modeling challenge. Initial POD modes can often be used to extract meaningful relationships between parameters of interest and a scalar of the flow field. However, later modes often vary in a more stochastic manner, leading to significant challenges in extracting meaningful interpolations. Results shown in this section highlight that even for low thrust rotors, an efficient representation can be drawn with a limited mode count. The second way by which a POD ROM may fail to produce accurate predictions is if interpolation predictions can not provide meaningful results for how these modes vary.

This failure can happen if a domain of interest is both too sparsely sampled and sufficiently non-linear. In the previous section, it was discussed how non-linearity in the data-set was increased for the low thrust case. In the next section, it will be shown how this non-linearity increase affects POD ROM prediction capabilities.

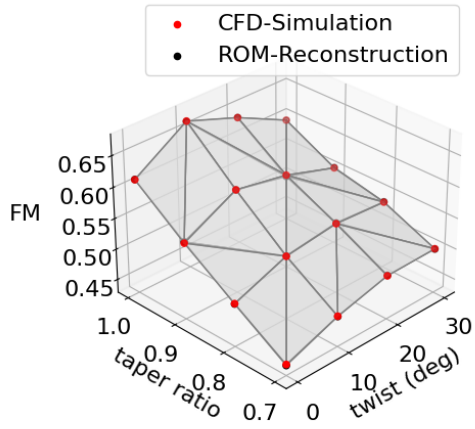

(a) FM

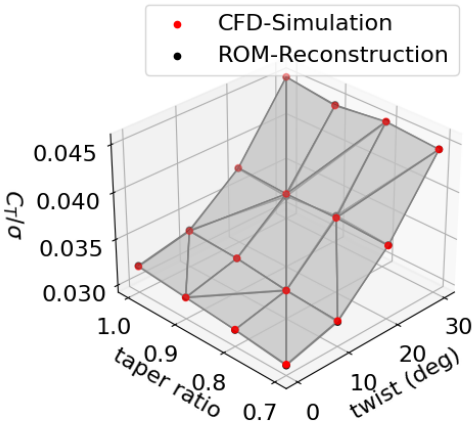

(b) $\frac{C_T}{\sigma}$

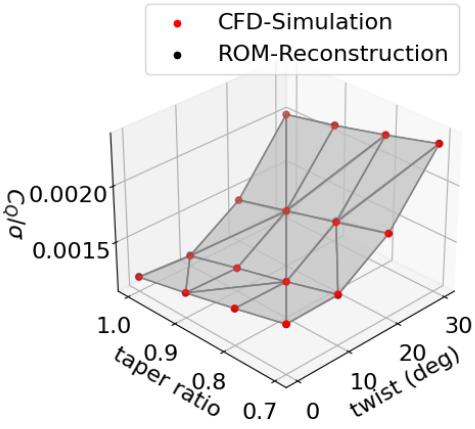

(c) $\frac{C_Q}{\sigma}$

Figure 13: Surface plot of FM, $\frac{C_T}{\sigma}$, and $\frac{C_Q}{\sigma}$ with respect to Ψ and λ as computed through CFD and POD ROM.

ROM Validation In observing percent error in surface pressure predictions for all three validation cases, two important observations were identified. It is shown that for validation case **v1**, surface pressure predictions were made with a high level of fidelity as shown in Figure 14a. Given that case **v1** only test for a change in Ψ, these results showed that POD ROM was capable of making highly accurate predictions under a variation in twist despite the noted increase in complexity for the low thrust rotor case. Results in Table 4 show that integrated load errors when predictions are made for only a variation in Ψ remain below 0.5%.

However, the same level of surface pressure prediction accuracy was not achieved for validation cases **v2** or **v3**. Results in Figure 14b and 14c show that when accounting for a variation in taper, λ, there is a significant increase in prediction error towards the rotor's tip for a low thrust rotor as compared to a high thrust rotor. This error results from the POD ROM not accurately modeling how rotor tip pressure distributions will vary with λ. While surface pressure prediction errors still never exceed a maximum of 1.5%, the increased area over which error occurs leads to a significant increase in integrated load error, raising FM prediction error from 0.77% and 0.37% for cases **v2** and **v3** of the high thrust rotor to 4.26% and 4.25% for the low thrust rotor.

Results of the low thrust rotor case show the capability of a POD ROM to make accurate load predictions is highly dependent on how well sampled is the domain of interest. By simply varying the rotor's collective this POD ROM is shown to have significant deterioration in prediction capabilities. This deterioration results not from a limitation in POD ROM reconstruction capability but rather through an under sampling of λ in the domain of interest. To construct a more accurate ROM, further sampling with new λ is required.

Yet, even with the limited sampling on the domain the POD ROM is still providing reasonably accurate predictions once accounting for the massive reduction in computational expense in evaluating each validation case. Prediction of surface pressures through POD ROM are completed in 10^{-5} seconds on a single core. In addition, results shown in Figure 11 show that local maximum for FM is found for a λ=1.0. This implies design optimization of blade's topology is largely an optimization of Ψ. As such, it was still feasible that this POD ROM could be leveraged to undergo a design optimization. The same design optimization algorithm and initial condition used for the high thrust rotor case was utilized. Results showed that a local optimal solution for twist and taper could be found at $\Psi = 11.5^\circ$ and $\lambda = 1.0$ while taking 1 minute of compute time on a single core. This optimal solution was found using 20 iterations. Despite the known limitations of the POD ROM, this case still shows that with reasonable accuracy a design space can be once again sampled and a ROM can be derived such that design variables can be optimized. To greater increase accuracy, further sampling of the design space is needed with respect to λ.

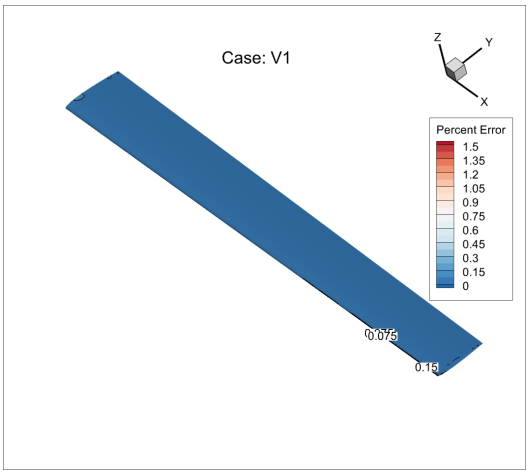

(a) **v1**

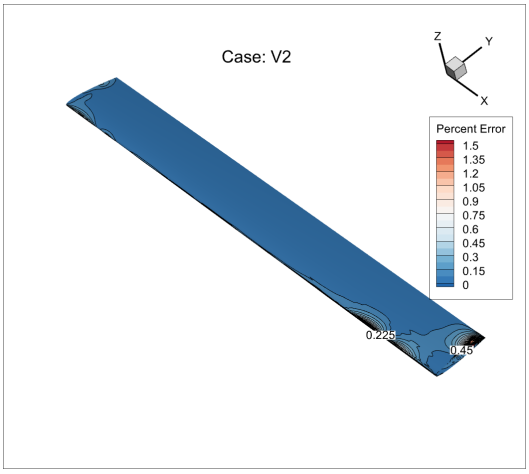

(b) **v2**

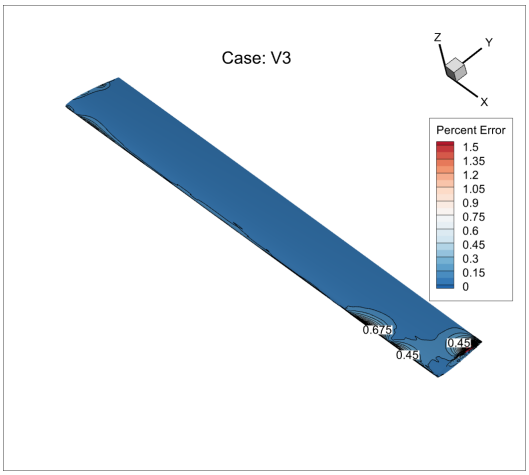

(c) **v3**

Figure 14: Percent error distributions for POD ROM surface pressure predictions with respect to CFD with all three validation cases.

Forward Flight

Up to this point in the study, the focus has been placed on hovering rotor blades. Given that these cases would produce

Table 4: Summary of percent errors in coefficient of thrust, torque, and figure of merit predictions using POD ROM.

Geometries	C_T	C_Q	FM
v1	0.23%	0.15%	0.49%
v2	0.80%	2.94%	4.26%
v3	1.65%	1.69%	4.25%

a pressure distribution which was invariant to changes in azimuth, the study could limit modeling to a limited set of 16 blade pressure distributions. However, for practical implementation of POD ROMs it is essential to model cases where blade load distribution varies with azimuth angle. As such, in this section a POD ROM will be used for prediction of load distribution of a rotor in forward flight.

There are numerous challenges which may arise for extending the POD ROM to rotors in forward flight. The leading challenge could be an increase in non-linear relationship between design variables and surface pressures. As shown in Figure 15, case **c4** ($\lambda = 1.0, \Psi = 30^\circ$) and case **c5** ($\lambda = 0.9, \Psi = 0^\circ$) have widely differing C_T distributions between azimuth of 0°-60° and a spanwise position up to r/R=0.50. This variation is a result of flow separation occuring as the blade travels counter clockwise past zero azimuth position. From Figure 15 it can be seen that through varying of taper and twist ratio, degree to which flow will separated will vary greatly. This flow separation and reattachment provides a significant increase in data-set complexity which could potential exacerbate the issue of POD ROM either not having enough sample points to making meaningful interpolations or not being capable of representing the system with low mode retention counts. The later of these issues will be addressed in the next section.

ROM Reconstruction After undergoing the POD algorithm it was identified that for a rotor in forward flight, 16 POD modes were required to obtain a mode retention count independent solution. Reconstructions and reconstruction error can be found in Figures 16 and Figures 17. This observation provides two important conclusions. First through an addition of flow separation and a varying azimuth angle, energy content in the training data-set has been expanded. This expansion in energy content has lead to an increase in required mode retention count to obtain independent reconstructions.

The second important observation is that despite the expansion in energy content, POD is shown to be capable of representing the full rotor disks of all 16 geometries with only 16 modes. For accurate reconstructions, modes retained were limited to modes with reasonably smooth variation with respect to Ψ and λ. These results highlight that the POD algorithm appears to be exceptionally well suited for applications modeling periodic pressure distributions of rotors. Maximum percent error of C_T found for reconstructions of all 16 geometries was found to be below 0.1%. In the following section, the effect of increased distributed load complexity on POD ROM prediction capabilities will be demonstrated.

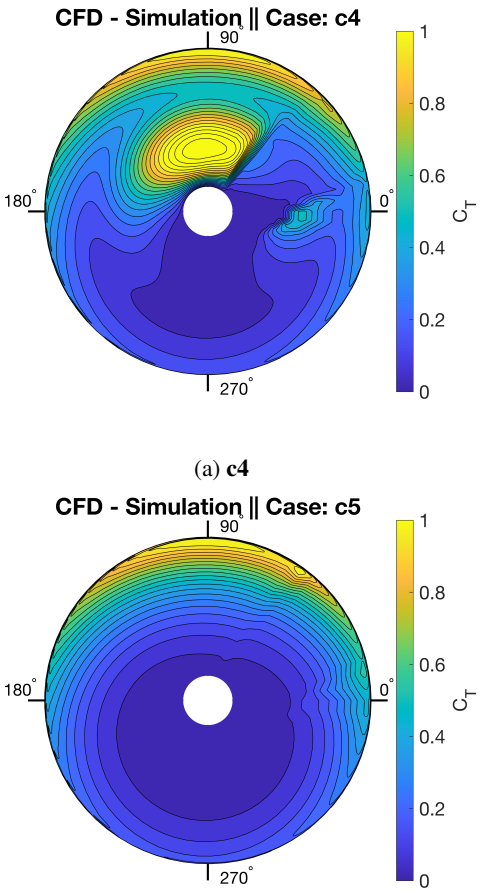

(a) **c4**

(b) **c5**

Figure 15: Contours of rotor's C_T as the blade rotates from an azimuth of 0° to 360°. Incoming flow is entering from the 180° direction while blade is rotating counter clockwise.

ROM Validation Both prediction and error contours of the rotor disk for all 3 validation geometries are summarized in Figures 18 and 19. The first important observation is that POD ROM is making highly accurate predictions for C_T across the rotor's complete cycle. Both separation and reattachment of flow is captured with a high degree of accuracy within each validation case. Of additional importance is the observation that despite large variations in rotor disk C_T contours, the POD ROM is still shown capable of making highly accurate predictions with maximum percent error remaining below 0.5% for all 3 cases.

This observation underlines the two critical takeaways from this study. First, if a modal decomposition algorithm is to be deployed for surface pressure modeling it must be capable of efficiently representing a complex domain. In this study, it has been shown that for a wide variety of operating conditions the POD algorithm has shown to perform exceptionally well at representing rotor surface pressures with minimum mode retention counts.

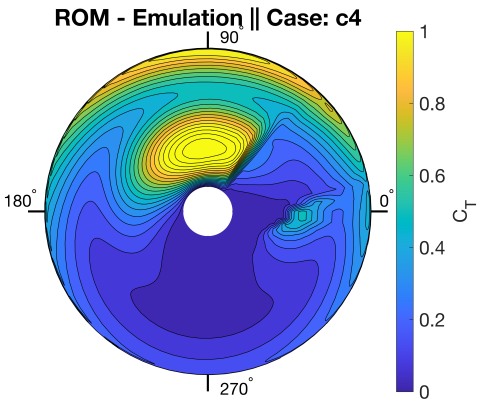

(a) **POD Reconstruction for c4**

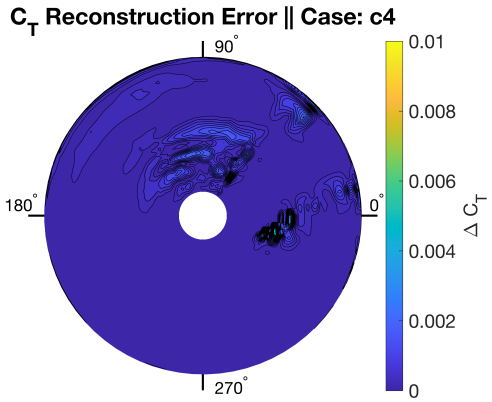

(b) **POD Error for c4**

Figure 16: Contours of POD reconstruction and error for C_T as the blade rotates from an azimuth of 0° to 360°. Incoming flow is entering from the 180° direction while blade is rotating counter clockwise.

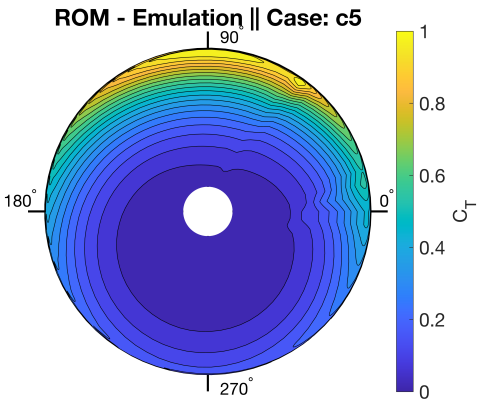

(a) **POD Reconstruction for c5**

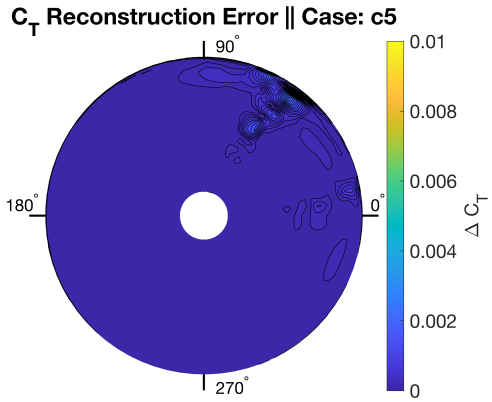

(b) **POD Error for c5**

Figure 17: Contours of POD reconstruction and error for C_T as the blade rotates from an azimuth of 0° to 360°. Incoming flow is entering from the 180° direction while blade is rotating counter clockwise.

The second observation is that for application of POD ROM to rotor surface pressure modeling, a sub-space must be sufficiently sampled such that the influence of design variables on load distributions is fully captured. It is important to note that prior knowledge of a system, particularly when applied to UAM aircraft, may be limited. As such, prior understanding of required sample size may not be held and an iterative approach must be taken to find sufficient sampling size required for a POD ROM. When investigating the high thrust rotor, this study found that 16 samples were sufficient to providing near exact predictions for surface pressures. Yet, when considering the low thrust rotor it was identified that while efficient reconstructions could be made through POD, more sampling conditions were required for accurate interpolations. This was due to an increase in design space complexity with respect to λ.

For the case of rotor in forward flight it was found that, similar to high thrust rotors, the design space could be represented exceptionally well with the 16 sampling cases. Yet, a deeper analysis of POD modes demonstrates that the total number of CFD sampling cases required to model the rotor's disk could be further reduced. Results for both POD ROM predictions and errors when using just 4 sampling cases (cases **c1**,**c4**,**c13**, and **c16**) is shown in Figures 20 and 21. In Figure 22, variation of POD modes 1, 2, and 8 with respect to Ψ and λ are plotted. For the first 2 POD modes, a comparable representation of mode variation can be made through both linear and spline based interpolations. This information means that high energy POD modes for rotor in forward flight are largely linear varying modes in this specific design space. It is not until mode counts 8 and up that mode relationship to design variables becomes more non-linear. Yet, given disparity in energy content between initial modes and later modes it can be shown that through only sampling the 4 cornering locations of the design space, thus producing only a linear mapping, a highly accurate model can still be produced. In Figure 21, errors are presented for all 3 validation cases once only 4 sampling conditions are used. Maximum percent error for these cases is 1.5%. POD ROM evaluation of rotor surface pressures across the entire periodic motion took 0.6 seconds on a single core. CFD simulation required 20 hours on 440 cores.

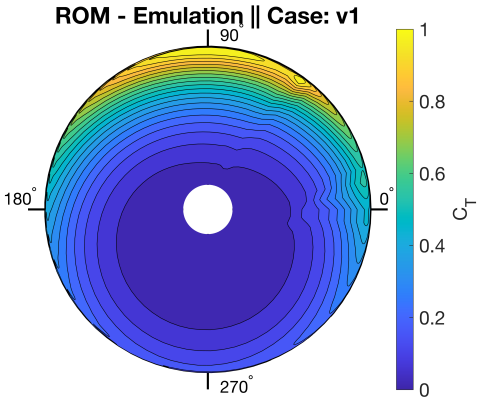

(a) **Case v1 Prediction**

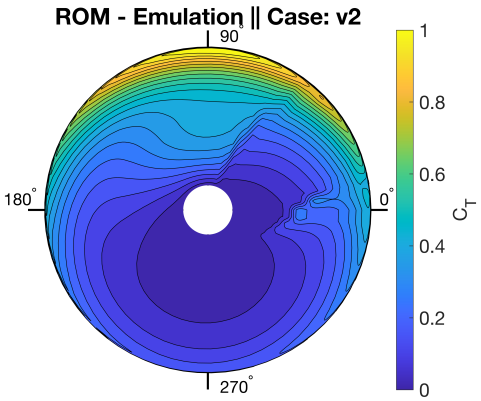

(b) **Case v2 Prediction**

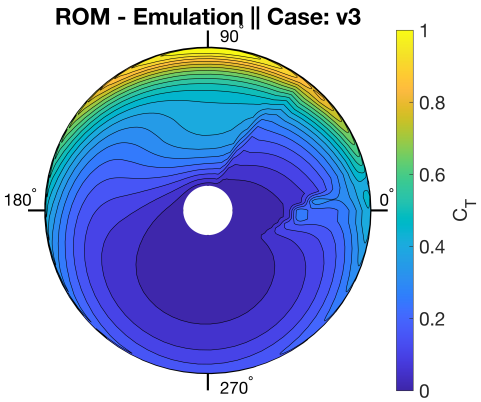

(c) **Case v3 Prediction**

Figure 18: Contours of POD ROM prediction using 16 sample cases for rotor's C_T as the blade rotates from an azimuth of 0° to 360°. Incoming flow is entering from the 180° direction while blade is rotating counter clockwise.

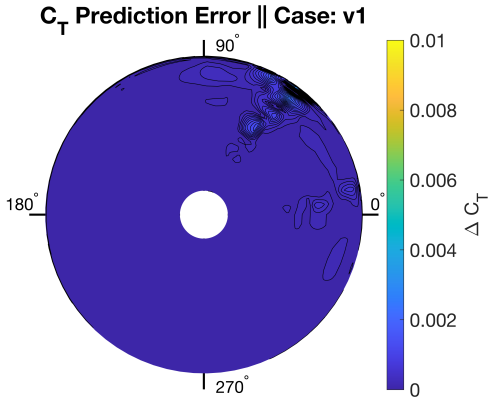

(a) **Case v1 Error**

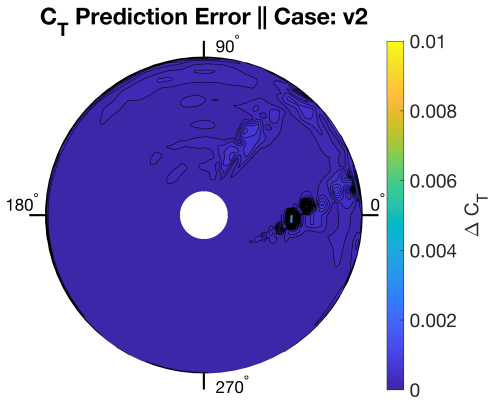

(b) **Case v2 Error**

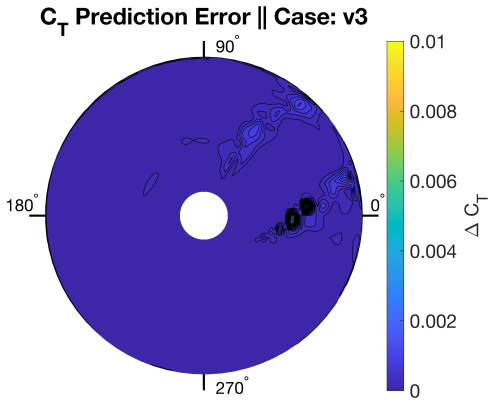

(c) **Case v3 Error**

Figure 19: Contours of error in POD ROM predictions using 16 sample cases for rotor's C_T as the blade rotates from an azimuth of 0° to 360°. Incoming flow is entering from the 180° direction while blade is rotating counter clockwise.

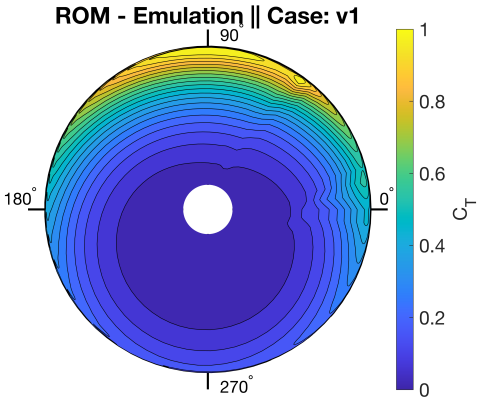

(a) **Case v1 Prediction**

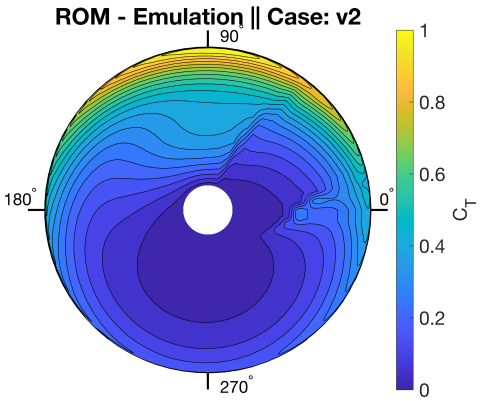

(b) **Case v2 Prediction**

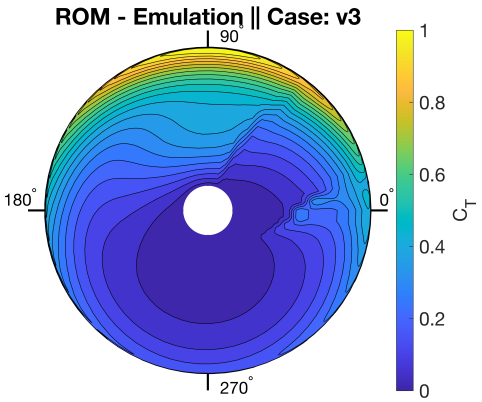

(c) **Case v3 Prediction**

Figure 20: Contours of POD ROM prediction using 4 sample cases for rotor's C_T as the blade rotates from an azimuth of 0° to 360°. Incoming flow is entering from the 180° direction while blade is rotating counter clockwise.

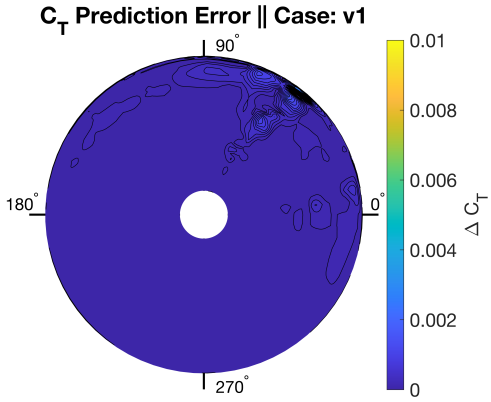

(a) **Case v1 Error**

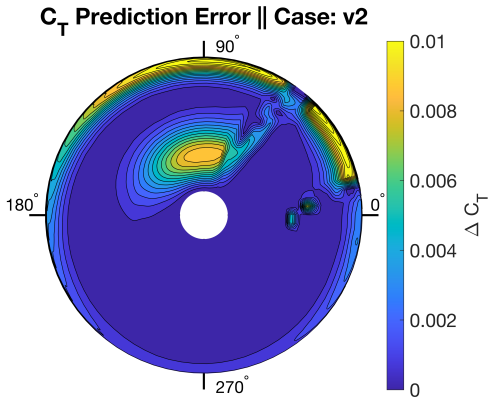

(b) **Case v2 Error**

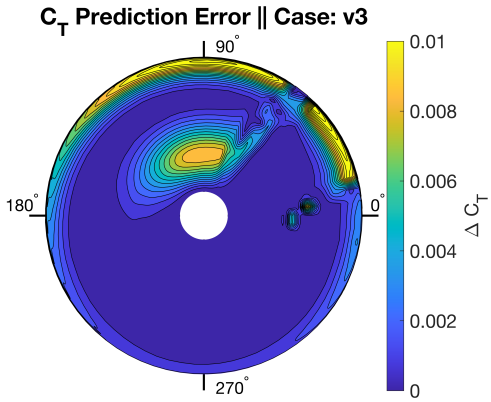

(c) **Case v3 Error**

Figure 21: Contours of error in POD ROM predictions using 4 sample cases for rotor's C_T as the blade rotates from an azimuth of 0° to 360°. Incoming flow is entering from the 180° direction while blade is rotating counter clockwise.

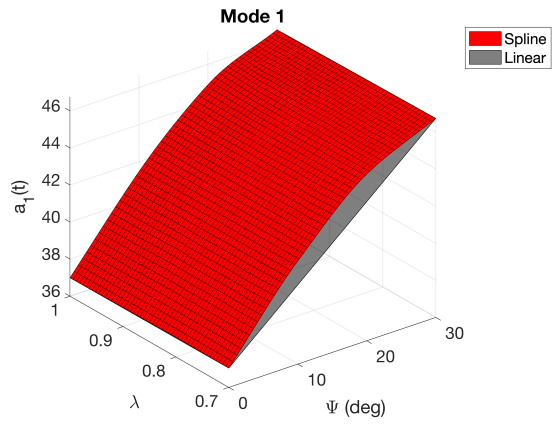

(a) **POD mode 1**

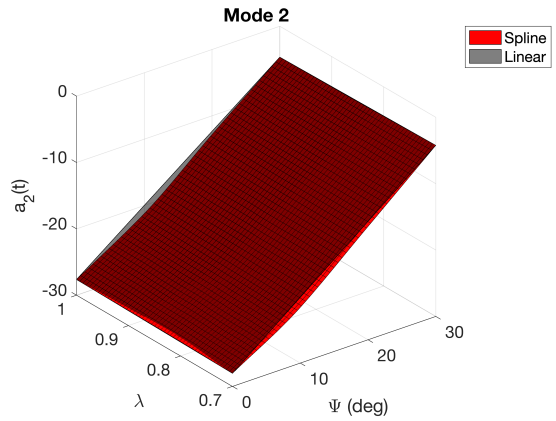

(b) **POD mode 2**

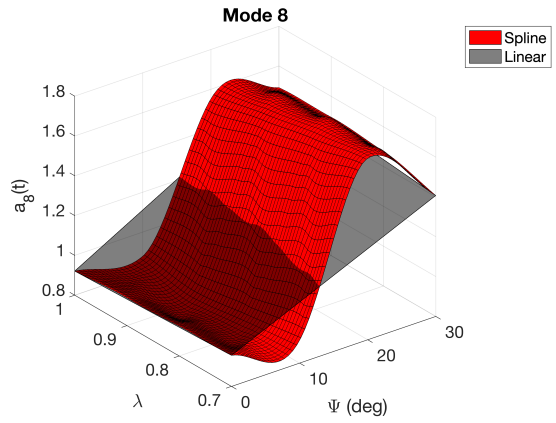

(c) **POD mode 8**

Figure 22: Surface plots showing both linear and spline representation of POD modes 1, 2, and 8.

CONCLUSIONS

In this study a POD ROM was applied to 3 demonstration cases for distributed pressure load predictions. Namely, these cases were high thrust hovering rotor, low thrust hovering rotor, and rotor in forward flight. For each of these cases, blade twist and taper ratio was varied such that 16 blade geometries were used. OVERFLOW CFD simulation solutions of these blades were then used to derive an interpolation based POD ROM. All three POD ROMs were shown to produce highly accurate predictions for surface pressure distributions. For both high thrust rotor and forward flight ROMs, maximum integrated load coefficient prediction error was below 1%. Error was increase for low thrust rotor ROM, but still limited to below 4.3%. When POD ROM was implemented, computational expense was significantly decreased. For hovering rotor, expense was reduced from 12 hours on 440 cores for CFD simulation to just 10^{-5} seconds on a single core for ROM predictions. For forward flight rotor, expense was reduced from 20 hours on 440 cores to 0.6 seconds on a single core when POD ROM was implemented. Expense was reduced to the extend that a design optimization became feasible for the high thrust and low thrust rotor cases. Results demonstrated how a POD ROM could be efficiently derived and deployed to model a complex design space to a high degree of fidelity and leveraged to quickly find optimal design points within the space.

While the present work provides strong evidence for feasible application of POD ROMs to rotorcraft, there are still several future steps remaining for understanding POD ROM limitations in rotorcraft modeling. POD ROM modeling of more realistic geometries should be attempted. Future steps should also be taken to include rotors operating in multi-rotor configurations. Additionally, CFD simulations should be completed using more complex operating conditions, such as pitch up maneuvers and flight in turbulent flow patterns. By including these two modeling choices a more broad range of length scales will be introduced into the training data-set thus testing POD ROMs capability for efficiently extracting meaningful information in more complex domains.

REFERENCES

1. W. Johnson, "CAMRAD II, Comprehensive Analytical Model of Rotorcraft Aerodynamics and Dynamics," *Johnson Aeronautics, Palo Alto, California*, vol. 1999, 1992.

2. H. Saberi, M. Khoshlahjeh, R. A. Ormiston, and M. J. Rutkowski, "Overview of RCAS and Application to Advanced Rotorcraft Problems," in *American Helicopter Society 4th Decennial Specialists' Conference on Aaeromechanics, San Francisco, CA*, 2004.

3. T. Quackenbush, D. Wachspress, A. Boschitsch, and T. Curbishley, "A Comprehensive Hierarchical Aeromechanics Rotorcraft Model (CHARM) for General Rotor/Surface Interaction," *CDI Report*, pp. 99–03, 1999.

4. J. C. Ho and H. Yeo, "Rotorcraft Comprehensive Analysis Calculations of a Coaxial Rotor with Lift Offset," *International Journal of Aeronautical and Space Sciences*, vol. 21, no. 2, pp. 418–438, 2020.

5. S. Conley and D. Shirazi, "Comparing Simulation Results from CHARM and RotCFD to the Multirotor Test Bed Experimental Data," in *AIAA Aviation 2021 Forum*, p. 2540, 2021.

6. S. J. Wright, "Fundamental Aeroelastic Analysis of an Urban Air Mobility Rotor," in *VFS's 9th Biennial Autonomous VTOL Technical Meeting*, 2021.

7. H. Yeo, J. Bosworth, C. Acree Jr, and A. R. Kreshock, "Comparison of CAMRAD II and RCAS Predictions of Tiltrotor Aeroelastic Stability," *Journal of the American Helicopter Society*, vol. 63, no. 2, pp. 1–13, 2018.

8. V. K. Lakshminarayan, J. Sitaraman, and A. M. Wissink, "Application of Strand Grid Framework to Complex Rotorcraft Simulations," *Journal of the American Helicopter Society*, vol. 62, no. 1, pp. 1–16, 2017.

9. M. Morelli, T. Bellosta, and A. Guardone, "Development and Preliminary Assessment of the Open-Source CFD Toolkit SU2 for Rotorcraft Flows," *Journal of Computational and Applied Mathematics*, vol. 389, p. 113340, 2021.

10. M. Nuernberg and L. Tao, "Three Dimensional Tidal Turbine Array Simulations using OpenFOAM with Dynamic Mesh," *Ocean Engineering*, vol. 147, pp. 629–646, 2018.

11. J. Smagorinsky, "General Circulation Experiments with the Primitive Equations: I. The Basic Experiment," *Monthly Weather Review*, vol. 91, no. 3, pp. 99–164, 1963.

12. P. R. Spalart, "Comments on the Feasibility of LES for Wings, and on a Hybrid RANS/LES Approach," in *Proceedings of first AFOSR international conference on DNS/LES*, Greyden Press, 1997.

13. T. Fitzgibbon, M. Woodgate, and G. Barakos, "Assessment of Current Rotor Design Comparison Practices based on High-Fidelity CFD Methods," *Aeronautical Journal*, vol. 124, no. 1275, pp. 731–766, 2020.

14. A. Abhishek, S. Ananthan, J. Baeder, and I. Chopra, "Prediction and Fundamental Understanding of Stall Loads in UH-60A Pull-Up Maneuver," *Journal of the American Helicopter Society*, vol. 56, no. 4, pp. 1–14, 2011.

15. C. Crozon, R. Steijl, and G. Barakos, "Coupled Flight Dynamics and CFD-Demonstration for Helicopters in Shipborne Environment," *Aeronautical Journal*, vol. 122, no. 1247, pp. 42–82, 2018.

16. R. Chau, "Process and Packaging Innovations for Moore's Law Continuation and Beyond," in *2019 IEEE International Electron Devices Meeting (IEDM)*, pp. 1–1, IEEE, 2019.

17. H. Wang and Z. J. Zhai, "Advances in Building Simulation and Computational Techniques: A Review Between 1987 and 2014," *Energy and Buildings*, vol. 128, pp. 319–335, 2016.

18. S. Neerarambam, P. O. Bowles, B.-Y. Min, D. Lamb, A. F. Dunn, J. Frydman, G. Harrington, C. Lian, M. Kazlauskas, B. E. Wake, *et al.*, "An Overview of the Exhaust Gas Reingestion Challenges on the CH 53K King Stallion," in *AIAA Scitech 2021 Forum*, p. 0028, 2021.

19. M. Colella, F. Saltari, M. Pizzoli, and F. Mastroddi, "Sloshing Reduced-Order Models for Aeroelastic Analyses of Innovative Aircraft Configurations," *Aerospace Science and Technology*, vol. 118, p. 107075, 2021.

20. H. Liu, X. Gao, Z. Chen, and F. Yang, "Efficient Reduced-Order Aerodynamic Modeling in Low-Reynolds-Number Incompressible Flows," *Aerospace Science and Technology*, p. 107199, 2021.

21. P. J. Schmid and J. L. Sesterhenn, "Decomposition Mode Decomposition of Numerical and Experimental Data," *Bull. Amer. Phys. Soc*, 2008.

22. M. Sieber, C. O. Paschereit, and K. Oberleithner, "Spectral Proper Orthogonal Decomposition," *Journal of Fluid Mechanics*, vol. 792, pp. 798–828, 2016.

23. X. Chen, L. Liu, T. Long, and Z. Yue, "A Reduced Order Aerothermodynamic Modeling Framework for Hypersonic Vehicles based on Surrogate and POD," *Chinese Journal of Aeronautics*, vol. 28, no. 5, pp. 1328–1342, 2015.

24. Y.-H. Chang, L. Zhang, X. Wang, S.-T. Yeh, S. Mak, C.-L. Sung, C. Jeff Wu, and V. Yang, "Kernel-Smoothed Proper Orthogonal Decomposition–Based Emulation for Spatiotemporally Evolving Flow Dynamics Prediction," *AIAA Journal*, vol. 57, no. 12, pp. 5269–5280, 2019.

25. Y. Jin, K. Lu, L. Hou, and Y. Chen, "An Adaptive Proper Orthogonal Decomposition Method for Model Order Reduction of Multi-Disc Rotor System," *Journal of Sound and Vibration*, vol. 411, pp. 210–231, 2017.

26. D. Cinquegrana and P. L. Vitagliano, "A Reduced Order Model for Boundary Layer Ingestion Map Prediction at Fan Inlet of Rear-Mounted Engine Nacelle," in *AIAA Scitech 2021 Forum*, p. 0993, 2021.

27. N. Peters, J. A. Ekaterinaris, and A. M. Wissink, "Mode Based Reduced Order Model for a Moving Store," in *AIAA Scitech 2021 Forum*, p. 0364, 2021.

28. N. Peters, J. Ekaterinaris, and A. Wissink, "A Mode Based Reduced Order Model for Supersonic Store Separation," in *AIAA Aviation 2021 Forum*, p. 2548, 2021.

29. N. Peters, J. Ekaterinaris, and A. Wissink, "A Mode Based Reduced Order Model for Rotorcraft Separation," in *AIAA Scitech 2022 Forum*, 2022.

30. K. Yonekura and K. Suzuki, "Data-Driven Design Exploration Method using Conditional Variational Autoencoder for Airfoil Design," *Structural and Multidisciplinary Optimization*, vol. 64, no. 2, pp. 613–624, 2021.

31. D. Zettl, E. Dreyer, B. Grier, J. J. McNamara, and C. L. Pasiliao, "Rapid Steady-State Pressure Prediction for Ultra High-Speed Vehicles," in *15th Dynamics Specialists Conference*, p. 1323, 2016.

32. P. G. Cizmas and A. Palacios, "Proper Orthogonal Decomposition of Turbine Rotor-Stator Interaction," *Journal of Propulsion and Power*, vol. 19, no. 2, pp. 268–281, 2003.

33. P. Buning, I. Chiu, S. Obayashi, Y. Rizk, and J. Steger, "Numerical Simulation of the Integrated Space Shuttle Vehicle in Ascent," in *15th Atmospheric Flight Mechanics Conference*, p. 4359, 1988.

34. W. Johnson, "NDARC-NASA Design and Analysis of Rotorcraft," tech. rep., 2015.

35. P. P. Walatka, *PLOT3D User's Manual*, vol. 101067. NASA, 1990.

36. W. M. Chan, "Advances in Software Tools for Pre-Processing and Post-Processing of Overset Grid Computations," in *Proceedings of the 9th International Conference on Numerical Grid Generation in Computational Field Simulations*, 2005.

37. S. Rogers, H. Cao, and T. Su, "Grid Generation for Complex High-Lift Configurations," in *29th AIAA, Fluid Dynamics Conference*, p. 3011, 1998.

38. J. Benek, J. Steger, F. Dougherty, and P. Buning, "Chimera. A Grid-Embedding Technique," 1986.

39. C. I. T. Chan, W. M. and P. G. Buning, "User's Manual for the HYPGEN Hyperbolic Grid Generator and the HGUI Graphical User Interface," *NASA TM-108791*, 1993.

40. R. Nichols, R. Tramel, and P. Buning, "Solver and Turbulence Model Upgrades to OVERFLOW 2 for Unsteady and High-Speed Applications," in *24th AIAA Applied Aerodynamics Conference*, p. 2824, 2006.

41. P. Spalart and S. Allmaras, "A One-Equation Turbulence Model for Aerodynamic Flows," in *30th Aerospace Sciences Meeting and Exhibit*, p. 439, 1992.

42. A. M. Wissink, J. Sitaraman, B. Jayaraman, B. Roget, V. K. Lakshminarayan, M. A. Potsdam, R. Jain, A. Bauer, and R. Strawn, "Recent Advancements in the Helios Rotorcraft Simulation Code," in *54th AIAA Aerospace Sciences Meeting*, p. 0563, 2016.

43. V. Sankaran, J. Sitaraman, A. Wissink, A. Datta, B. Jayaraman, M. Potsdam, D. Mavriplis, Z. Yang, D. O'Brien, H. Saberi, *et al.*, "Application of the Helios Computational Platform to Rotorcraft Flow Fields," *AIAA paper*, vol. 1230, p. 2010, 2010.

44. A. M. Wissink, B. Jayaraman, S. A. Tran, R. Jain, M. A. Potsdam, J. Sitaraman, B. Roget, and V. K. Lakshminarayan, "Assessment of Rotorcraft Download Using Helios v8," in *2018 AIAA Aerospace Sciences Meeting*, p. 0026, 2018.

45. P. Anusonti-Inthra, "Full Vehicle Simulations for a Coaxial Rotorcraft using High-Fidelity CFD/CSD Coupling," in *2018 AIAA Aerospace Sciences Meeting*, p. 0777, 2018.

46. J. C. Ho, B. Jayaraman, and H. Yeo, "Coupled Computational Fluid Dynamics and Comprehensive Analysis Calculations of a Gimballed Tiltrotor," *AIAA Journal*, vol. 57, no. 10, pp. 4433–4446, 2019.

47. K. Pearson, "LIII. On Lines and Planes of Closest Fit to Systems of Points in Space," *The London, Edinburgh, and Dublin Philosophical Magazine and Journal of Science*, vol. 2, no. 11, pp. 559–572, 1901.

48. P. Holmes, J. L. Lumley, G. Berkooz, and C. W. Rowley, *Turbulence, Coherent Structures, Dynamical Systems and Symmetry*. Cambridge university press, 2012.

49. L. Sirovich, "Quarterly of Applied Mathematics," *XLV*, vol. 3, 1987.

50. S. L. Brunton and J. N. Kutz, *Data-Driven Science and Engineering: Machine Learning, Dynamical Systems, and Control*. Cambridge University Press, 2019.